Validating mechanistic models of fluid displacement during imbibition

Sharon Ellman[1,2] – email address: sharon.ellman@ugent.be

Arjen Mascini[1,2] – email address: arjen.mascini@ugent.be

Tom Bultreys[1,2]– email address: tom.bultreys@ugent.be

[1]PProGRess,Dept. of Geology, Ghent University, Krijgslaan 281/ S8, 9000 Ghent, Belgium

[2]Centre for X-ray Tomography, Ghent University, Proeftuinstraat 86, 9000 Ghent, Belgium

This paper is a non-peer reviewed preprint submitted to EarthArXiv.

Validating mechanistic models of fluid displacement during imbibition

Sharon Ellman[1,2], Arjen Mascini[1,2] and Tom Bultreys[1,2]

[1]PProGRess,Dept. of Geology, Ghent University, Krijgslaan 281/ S8, 9000 Ghent, Belgium

[2]Centre for X-ray Tomography, Ghent University, Proeftuinstraat 86, 9000 Ghent, Belgium

Abstract:

Pore-scale modelling is an important tool to improve our understanding of multiphase flow in porous media. Slow fluid invasion is commonly modelled using quasi-static pore network models (PNM). These models simulate the invasion in a network of simplified pores and throats by invading network elements in order of the quasi-static "invasion" capillary pressure it would take for the wetting phase to enter. Despite a multitude of studies that address the predictiveness of PNM, it remains unclear what the leading causes of errors in these methods are, particularly during imbibition. To address this, we developed a novel method to directly validate the invasion capillary pressure models that underly quasi-static PNM for the first time. The new method compares these models to local capillary pressures measured during in-situ flow experiments visualized with 4D micro-CT. We applied this to two different PNM extractions from a µCT dataset of a glass beads pack that underwent slow imbibition. This methodology is limited by the temporal resolution of the data, hence we tested assumptions regarding displacement sequences when individual displacements could not be resolved. To constrain the uncertainty on the input parameters, we used local contact angles measured from the µCT images. The model-predicted invasion-Pc values were on average greater than the direct measurements made using curvatures also extracted from the µCT images. Important sources of mismatch were the difficulty to accurately describe the pore space as a network of pores and throats, as well as the relatively low temporal resolution of the dataset. The method and results presented here can be used to direct the development of improved pore network models.

I.INTRODUCTION

Multiphase flow in permeable materials is of vital importance to several issues facing the world at present. It is key to several geo-engineering challenges, such as contaminant transport and subsequent remediation[1,2], subsurface energy storage[3] and carbon dioxide sequestration[4,5]. Field-scale models attempt to predict fluid flows at the application scale. These large-scale models require constitutive properties as input, such as capillary pressure (Pc) and relative permeability curves. These properties are difficult to measure and the factors which control them (such as interfacial curvatures, contact angles, pore space morphology[6], etc.) are poorly understood[7]. To address these problems, significant research effort has been devoted to developing models which can predict the constitutive properties needed for field-scale models based on the microscopic, pore-scale properties of porous media samples.

Pore-scale multiphase flow modelling is challenging due to the need to track many complex fluid menisci as they move through the porous medium, giving rise to intricate patterns in how the fluids occupy the pores in the system[8,9]. These fluid occupation patterns play an important role in the constitutive properties needed for large-scale modelling. The need to capture pore scale fluid arrangements has given rise to the development of a range of different numerical methods, as reviewed in Bultreys et al.[10]. The two main categories are simplified pore networks and models that run directly on the pore space (i.e., direct approaches). These can be further broken up into quasi-

static and dynamic approaches[11]. Direct dynamic simulations solve the flow on a grid or mesh that captures the pore walls in as much detail as possible. They are typically based on the Lattice Boltzmann method or Navier-Stokes discretization approaches (e.g. finite volume methods)[12]. Due to their computational constraints, these methods are limited to small spatial and temporal domains, typically below that of fluid clusters, which is the scale needed to perform upscaling[7]. In pore network models (PNMs), on the other hand, the pore space is represented as a network of pores connected by throats, both with an idealized geometry[13]. Simplified rules governing the transport and arrangement of fluids are applied over the system so that macroscopic properties can be estimated[13]. This method's efficiency means it can be applied over relatively large spatial domains, though this comes at the cost of predictive capability and accuracy[12 14]. Because PNMs are simplifications of the process, using them can help us test our understanding of multiphase flow and whether the simplifications we imbue in them are reasonable or useful. This implies that they may be useful as tools to analyse which aspects of the studied processes require further investigation.

Despite the significant body of research on and with quasi-static PNMs in the last 30 years[7,15,16], one of the main outstanding questions is how well these models reproduce fluid displacements during multiphase flow. Recent studies have compared fluid distributions predicted by PNMs to pore-scale imaging experiments of drainage and imbibition (the displacement of a wetting phase by a non-wetting phase from the pores and vice versa), and mainly found discrepancies for imbibition[7,16]. The causes for these discrepancies have however been difficult to pin down from the fluid distributions alone, as these are only the outcome of the underlying displacement models employed by the PNM. Quasi-static PNMs simulate the filling of the pore space with an invading fluid by taking into account the pressure difference between the two fluids (the "capillary pressure" Pc) when the two fluids would be at equilibrium. The model assesses the Pc when different accessible pores would be invaded, and then chooses the option with the most beneficial invasion capillary pressure (i.e. the one closest to the current equilibrium). During drainage, this results in an incremental invasion from low to high invasion-Pc, while this order is reversed during imbibition[17]. The calculation of the invasion-Pc values thus controls the predicted sequence in which the invading fluid occupies the pore space, and thereby the fluid distribution patterns that emerge.

In this paper, we address the problem of validating quasi-static PNMs by developing a novel method to directly verify the underlying models that control fluid displacement, rather than only the resulting fluid distributions as performed in previous approaches[7,16]. Validating these invasion-Pc models on a displacement-by-displacement basis has not been done before now due to the difficulty of measuring local fluid-fluid curvatures (i.e. capillary pressure) during a fluid displacement experiment[18]. Obtaining local curvatures requires high resolution time-resolved µCT images[6,18] which has only recently become possible[19–22]. Another challenge to perform this validation has been the need to supply accurate fluid-fluid-solid contact angles to the displacement models. In PNM, contact angles have often been approached as tuning parameters to make the model fit measurements of core-scale constitutive properties, rather than as an independently measured microscopic property of the system. The techniques to measure contact angles inside porous media have only recently been developed[18,23–25]. This explains why it was previously only possible to validate PNMs using core-scale measurements[11,13,26] or µCT images of fluid distributions[7,16].

We use the novel invasion-Pc validation method to verify two different PNMs of imbibition on a µCT dataset of imbibition in a glass beads pack[27] in order to pin down the leading causes of error in these models. To do this, we extracted pore networks from the glass beads pack dataset, which we used to identify imbibition displacements. Next, we extracted the fluid menisci to determine curvatures on a displacement-by-displacement basis. Then, instead of assigning advancing contact

angles randomly from a range which is assumed reasonable as has been previously done when using PNMs[16,28–30], we measured a local advancing contact angle for each displacement directly from the µCT images. This has the potential to improve the predictive capabilities of PNMs[16,23,31,32]. These provided the inputs needed for the PNMs, which we then used to predict the invasion-Pc for each identified displacement. To validate the PNMs, we compared the predicted invasion-Pc values to Pc values determined from the curvatures of the fluid menisci. First, we briefly review pore-scale displacements and capillary pressures in Section II. Then we describe the experimental data in Section III.A, followed by an explanation of the methodology used in Section III.B and III.C. Next, we discuss the results from the contact angle measurements in Section IV.A and validation of the image-based curvatures in Section IV.B. We then discuss the results from the underlying models compared to the image-based values in Section IV.C. This is followed by conclusions in Section V.

II. Pore-scale displacements and capillary pressures

A. Types of displacements

Multiphase flow in the subsurface is typically slow, characterized by capillary numbers below 10^{-7}, and is hence assumed to be dominated by capillary forces[33]. Fluid flow therefore consists of sequences of discrete fluid displacements[34,35] interspersed with reversible movements such as film growth or menisci curvature changes[11,19]. When nonwetting fluid displaces wetting fluid, it is called drainage. This is a less complex displacement process than imbibition, which is when wetting fluid displaces nonwetting fluid[34]. The latter is studied in this work.

Imbibition occurs as a combination of piston-like displacements, cooperative pore-fillings and snap-offs[13]. Piston-like displacements occur when the wetting fluid displaces the nonwetting fluid in a pore which is connected to only sone throat filled with nonwetting fluid (Figure 1). This type of displacement does not change the connectivity of the fluid and is comparable to the Haines jumps[36] which occur during drainage.

A cooperative pore-filling occurs when the wetting fluid displaces the nonwetting fluid in a pore which is connected to two or more surrounding throats filled with nonwetting fluid. In these instances, the radius of curvature of the meniscus is larger than the single pore would dictate, as the interface extends partly into the involved throats (Figure 1). These events are classified in terms of fluid configurations by the I_n symbol, where 'n' represents the number of surrounding throats filled with nonwetting fluid as the displacement occurs[35].

Snap-off occurs when wetting fluid layers inside of throat corners swell due to the decreasing Pc, and eventually touch. This forms an unstable interface which rapidly expels nonwetting fluid from the throat, thereby "snapping off" the non-wetting phase connection between the two neighbouring pores. This alters the connectivity of the nonwetting fluid within the pore space[37] (Figure 1 C).

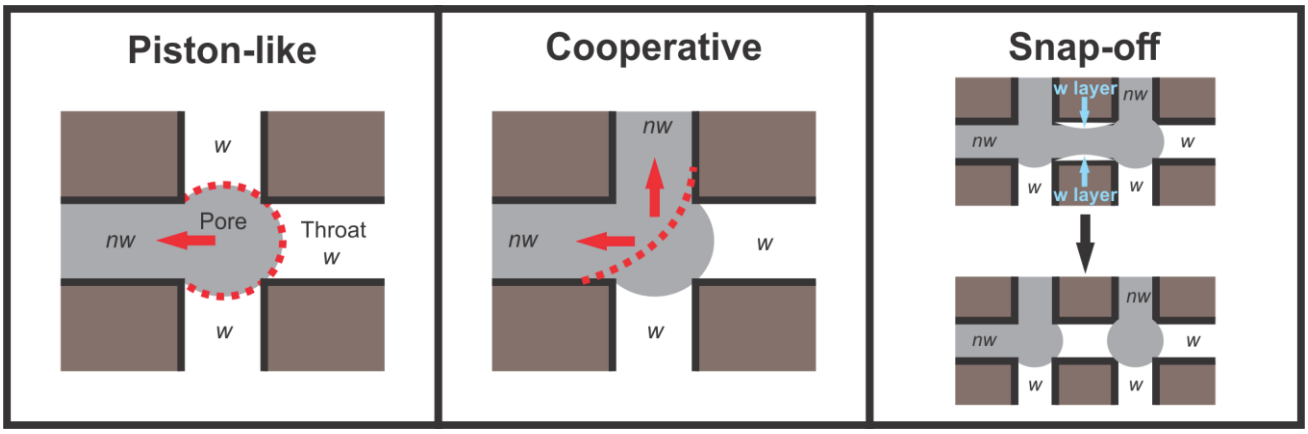

Figure 1: Left) Piston-like displacement; Middle) Cooperative pore-filling, specifically an I_2 displacement as two throats are filled with nonwetting fluid as the displacement occurs; Right) Snap-off. 'w' represents the wetting fluid and 'nw' represents the nonwetting fluid. These diagrams were adapted from Singh et al.[35].

B. Capillary pressure definitions

Large scale models need constitutive inputs which describe the flow, one of the most important of which is the macroscopic Pc[33]. This is the pressure difference between the nonwetting fluid and the wetting fluid measured over the whole sample, and is typically plotted against the average wetting saturation of the porous medium. The macroscopic Pc is an average of the microscopic (here referred to as local) Pc throughout the medium, which is the pressure difference across a meniscus at a certain point in the sample and at a given moment in time[33].

When the local Pc is at equilibrium, the fluid interface remains stationary. When the local Pc is above or below the equilibrium Pc, the meniscus, by definition, advances or recedes. During imbibition, when the local Pc reaches the lowest equilibrium Pc associated to a pore, (most of) the nonwetting fluid is suddenly evacuated from it[33]. This threshold value is referred to as the invasion-Pc. During capillary dominated flow, the invasion-Pc is therefore assumed to control the sequence in which fluid displacements occur[33].

C. Invasion percolation

Invasion percolation is an algorithm to approximate how fluids invade the pore space during capillary dominated two-phase flow[38]. At each point during the invasion of the network, the algorithm first looks for all accessible displacements – meaning that the wetting phase has a connected path to enter the network element and the non-wetting phase has a path to escape from it. The accessible displacement which corresponds to the highest invasion-Pc is then assumed to occur first[38]. This is because the macroscopic Pc is assumed to slowly decrease during imbibition. The opposite is true for drainage, where displacements corresponding to lower invasion-Pc values are assumed to occur first. In invasion percolation, the sequence in which fluid displacements occur is therefore controlled by the invasion-Pc. Following these rules, we find that smaller pores are invaded first during imbibition and that piston-like displacements and snap-offs are favoured as they occur at higher invasion-Pc values[35].

D. Invasion-Pc modelling

Different models are required to predict the quasi-static invasion-Pc values at which different types of imbibition displacements are expected to occur. These models are described below.

1. Piston-like displacements

During piston-like displacements, the wetting fluid invading the pore has only one path through which it can advance, hence the Young Laplace equation for cylindrical geometries (Equation 1) can be used to calculate the invasion-Pc by assuming the pore is locally cylindrical in shape[18]. θ is the advancing contact angle measured through the densest phase, r is the pore radius of the invaded pore and σ is the interfacial tension.

$$Pc = \frac{2\sigma\cos\theta}{r} \qquad \textit{Equation 1}$$

2. Cooperative pore-fillings

The geometry-based cooperative pore-filling model developed by Ruspini et al.[39] is the only quasi-static PNM algorithm which takes the local pore structure and fluid topology into account when determining cooperative pore-filling invasion-Pc values. The model accounts for the geometrical characteristics of the pore, the spatial distribution of the throats surrounding the invaded pore as well as the fluid topology at the moment of displacement. It assesses the filling states of the throats surrounding the invaded pore and trigonometrically calculates the curvature of the meniscus which matches the given advancing contact angle and the relative position of the throats (Figure 2). This curvature is then used to calculate the invasion-Pc for that pore. It is assumed that the pair of throats which are filled with nonwetting fluid and have the largest angular spacing govern the invasion-Pc. The equations to calculate the invasion-Pc from this information can be found in the supplementary material[40].

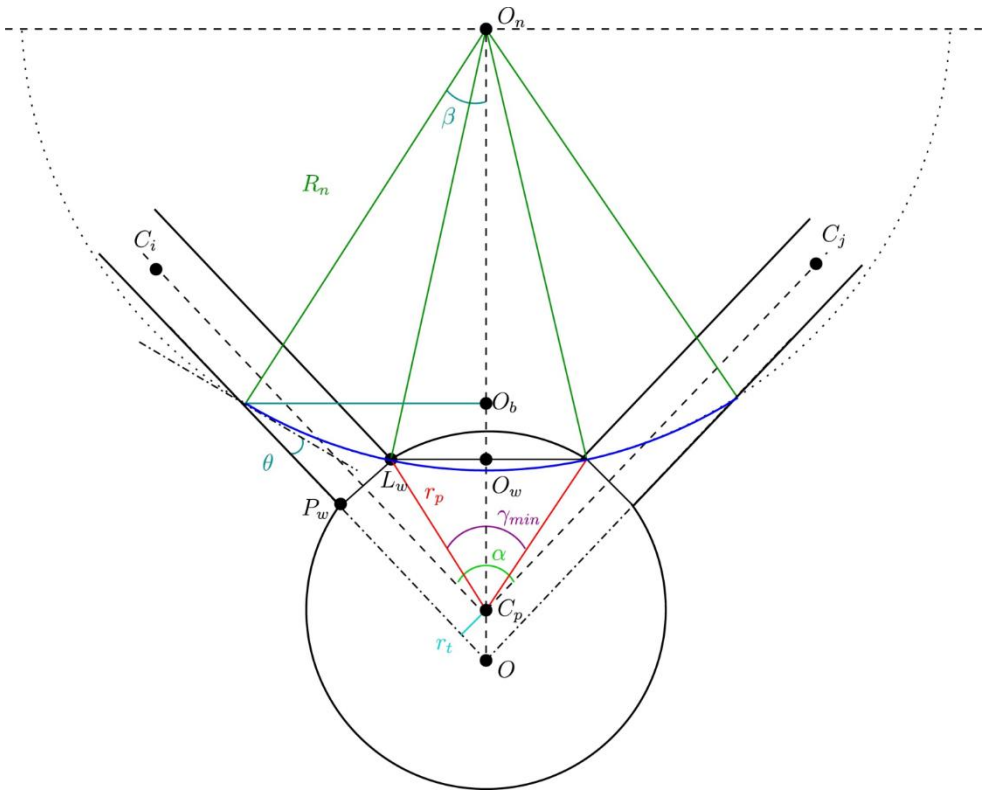

Figure 2: Geometrical description of an advancing fluid interface used in the cooperative pore-filling model[39]. For a description of the variables, see Ruspini et al.[39].

3. *Snap-off*

In order to calculate the invasion-Pc of snap-offs, the geometry of the throat and the advancing contact angle are used along with the distance that the arc menisci must travel before they meet and cause the instability that results in the snap-off[13]. To determine this distance, the model uses the receding contact angle as well as the maximum meniscus curvature reached during the preceding drainage. The throats are assumed to be triangular in cross-section. The equations to calculate the invasion-Pc from this information can be found in the supplementary material[40].

III.Materials and Methods

In Figure 3, we have a flowchart showing the workflow developed and used in this paper. The steps are elaborated on in this section.

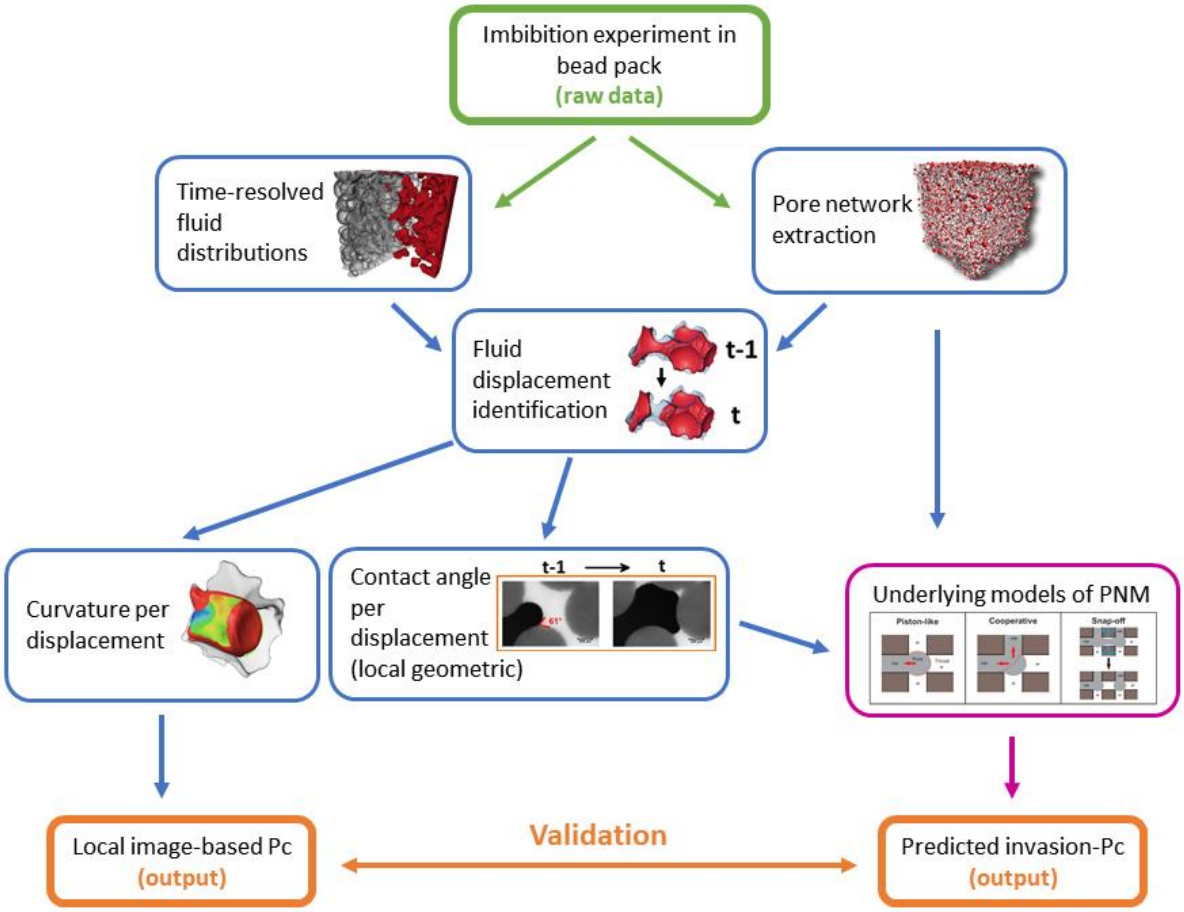

Figure 3: Workflow of the methodology used.

A. Experimental data

To verify imbibition PNMs, we compared model-predicted invasion-Pc values to fluid-fluid interfacial curvature measurements on µCT images of fluid distributions during imbibition. To do this, we assessed the Pc-values calculated from these curvatures (resulting in what we call 'local image-based Pc') and contact angle measurements in individual pores, determined from time-resolved µCT images. The experimental data came from an imbibition experiment in a glass beads pack performed by Schlüter et al[27]. The experiment was the unsteady-state injection of wetting fluid into a cylindrical sample containing nonwetting fluid, directly after primary drainage. This data set had a temporal

resolution high enough to identify most fluid displacements on a pore-by-pore basis and a spatial resolution high enough to resolve the curvature of the fluid menisci. It also contained external pressure transducer measurements, which we used to validate the curvature measurements. Capillary dominated flow was ensured by injecting at low flow rates. A summary of the experimental parameters can be found in Table 1. This time-resolved µCT experiment resulted in a series of 3D segmented images. Each image corresponds to the fluid distribution in the pore space at a discrete time during the experiment. We used the segmentation provided by Schlüter et al.[27], which was made with a modified form of Markov random field segmentation[27].

Table 1: Overview of the dataset used in the image analysis.

Parameter	Value
Sample Dimension	5.8 mm dia. X 7 mm long
Boundary condition	Constant flow rate
Fluids	n-dodecane, CsCl-brine
Interfacial tension	36 mN/m
Flow rate	20 µl/h
Capillary number	10^{-8}
Number of timesteps	52
Time per time step	113 s
Time span (hr:min:sec)	2:37:16
Reconstructed voxel size	8.4 µm
Pumped volume	54.1 µl
Reference	Schluter et al.[27]

B. Image analysis

We analysed the 3D segmented imbibition images to obtain a characterisation of the pore space geometry as well as local curvature and contact angle measurements. The workflow we used for the image analysis is inspired by the workflow for contact angle analysis during drainage described in Mascini et al.[18]. To test the invasion-Pc models discussed in Section II.D, two different pore network models were extracted from the dry scan of the sample. These same networks were used to identify fluid displacements in individual pores in the experiment, forming the basis for local contact angle and curvature measurements. The contact angles were then used as inputs for the PNMs described above, and the curvatures were used to compare the invasion-Pc predictions for the given pore geometry and contact angle to the experiment. This workflow is described in detail below.

1. Pore network extraction

The first step in the analysis was to divide the pore space into individual pores which are separated by narrower regions called throats. This was done using "pnextract" (an open source algorithm developed at Imperial College London[41]) as well as by using a watershed segmentation performed in Avizo 2020.3 (Thermo-Fisher Scientific) which was fed into the open source python package "porespy"[42] to produce the pore network. The largest inscribed spheres of the pores and the throats were found for both cases. The radii of the pores and throats were determined as the radii of the inscribed spheres in the pore and throat centre points. These pore network extractions served a dual purpose: firstly, they formed the basis of local fluid displacement detections, and secondly, they provided the pore space geometry characterisation needed as input for the PNMs.

2. Fluid displacement identification

In order to assess the filling states of the pores and throats, the inscribed spheres were overlaid on the imbibition dataset (after it was registered to the dry scan of the sample). The fluid occupancy of the centre (bulk) of each pore or throat was then determined by whether the majority of the voxels in its inscribed sphere were filled with wetting fluid or nonwetting fluid. We did this for every pore and

throat in every timestep, using Avizo 2020.3. A fluid displacement was then identified when the occupancy of a pore changed from nonwetting to wetting fluid in a certain time step. Connected pores which changed occupancy in the same timestep were grouped into the same fluid displacement (Figure 4). This was done in MATLAB using a graph-based connectivity clustering of the pores filled in each timestep. The pores and throats neighbouring the displacement were also recorded. The source pore for each displacement was assumed to be the pore within the invaded region with the largest radius. This works under the assumption that the pore where the meniscus started to move through first will be the pore corresponding to the lowest invasion-Pc in a certain multi-pore displacement. In an invasion-percolation framework, this is the pore which determines the invasion-Pc, hence the radius of this pore is used in the PNM-based invasion-Pc models. Once the displacements were identified, they were then classified as piston-like displacements or cooperative pore-fillings, by assessing the occupancy of the throats surrounding the displacement in the timestep prior to its occurrence. Snap-offs in throats were identified as throats which changed occupancy while their two neighbouring pores remained filled with nonwetting fluid. The result of the fluid displacement identification was a list of categorised imbibition displacements with accompanying details on time and location at which they occurred, surrounding pores, etc.

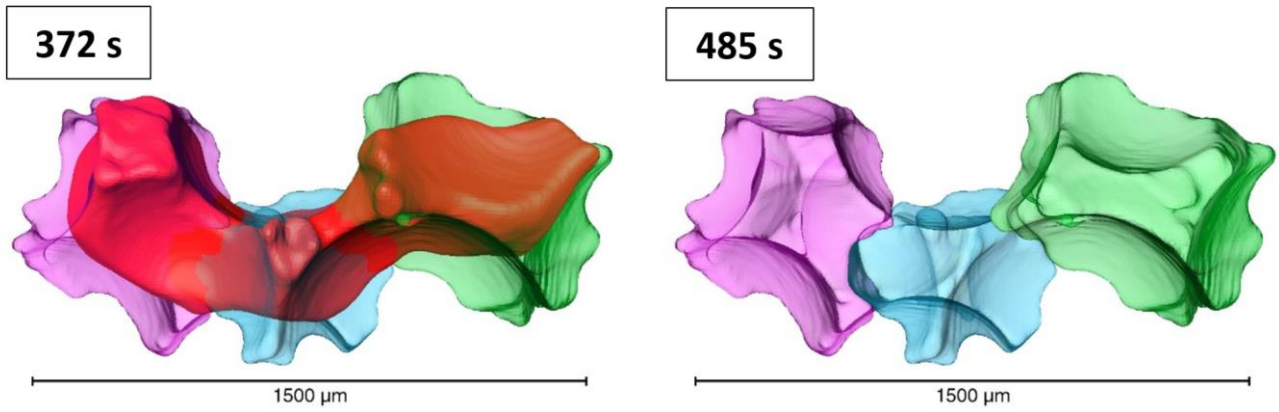

Figure 4: An example of a multi-pore event. The three pores are transparent and are coloured in pink, blue and green (all grey in black and white), while the opaque red (dark grey in black and white) is the oil. At 372 s, the pores are filled with oil, while at 485 s the oil has been displaced by brine. Since the oil was displaced from all three pores in the same timestep, they were classified as a single displacement. These times represent consecutive scans taken during the experiment.

3. Curvature measurements

To determine the curvature of the fluid menisci, the fluid/fluid interface was extracted as a triangulated surface from the three-phase segmented image at each timestep, using the marching cubes algorithm in Avizo 2020.3[43]. Consequently, constrained smoothing using a Gaussian filter with a smoothing extent of three voxels was performed in Avizo 2020.3. This method is analogous to that of Li et al.[44]. The mean surface curvature was then determined from the Eigenvectors and Eigenvalues of a quadratic form which was locally fitted to the extracted surface. The image resolution limits the accuracy of this computation, especially in regions where the partial volume effect is especially pronounced, such as near the three-phase-contact-line[6]. To account for this, the data points were filtered based on two criteria. First, all curvatures corresponding to a radius of curvature smaller than 2 voxel sizes were omitted as these most likely represented noise. Then, data points were filtered based on their geodesic distance to the edge of the surface, i.e. points closer than 20% of the maximum geodesic distance were omitted. These distances were determined using the shortest edge distance algorithm[45]. Within each pore, the remaining datapoints were then weighted based on their geodesic distance (points further away from the grain surface were given a greater weighting) and the mean curvature per pore per timestep was calculated. To find the local curvature as closely as possible before

a filling event (i.e. a meniscus reconfiguration), we averaged the curvatures in the pores in the displacement as well as in the neighbouring pores in the time step immediately prior to its occurrence. This resulted in a single curvature estimate for each displacement.

4. Contact angle determination

Wettability, which is characterised by contact angle, has been found to vary in space, even within homogeneous materials such as that used in this study[46]. Our aim was to validate predictions of the invasion-Pc of individual fluid displacements, which depend in part on the effective contact angle of that specific displacement. This is why using a method which measures contact angles locally within the pore space was necessary. We compared several methods to measure contact angles locally both in space and time on time-resolved images of the fluid distributions to find the most suitable for use in the PNMs. These methods are briefly summarized below.

(a) Geometric contact angles. Geometric contact angles were first measured on micro-CT data by Andrew et al.[23], where the angle between the fluid/fluid interface and the solid surface was measured manually in the plane perpendicular to the three-phase-contact-line. This method was then enhanced by automated algorithms which find the geometric contact angle at every point on the three-phase-contact-line in the entire pore space[24,31,32,47]. We used the code developed by AlRatrout et al.[24] to calculate the conventional geometric contact angle distribution, which was determined from a single 3D image at the end of imbibition.

The local geometric contact angle introduced by Mascini et al.[18] yields geometric contact angles locally in space and time. In this method, the code of AlRatrout et al.[24] is used in conjunction with a pore separation to determine a geometric contact angle in individual pores at the moment just before a fluid displacement takes place. This method was shown to reduce the uncertainty linked to the state of the interface caused by contact angle pinning. For a detailed description of the method, see Mascini et al.[18].

(b) Force-based contact angles. Force-based contact angles were first defined by Mascini et al.[18] as a method of identifying the effective contact angle linked to drainage fluid displacements or piston-like imbibition displacements. The Young-Laplace equation provides a link between the meniscus curvature and the contact angle associated to the displacement, if the radius and shape of the invaded pore is known (see Equation 2). In Equation 2, σ is the interfacial tension, k_{thr} is the threshold curvature, θ_f is the force-based contact angle and r is the radius of the invaded pore. This equation makes the assumption that the invaded pore is cylindrical in shape.

$$2\sigma k_{thr} = \frac{2\sigma \cos\theta_f}{r} \qquad \textit{Equation 2}$$

(c) Thermodynamic contact angles. By extending the work of Blunt et al.[48] and Mascini et al.[18], the thermodynamic contact angle for each imbibition displacement was determined using Equation 3. This contact angle definition works by assuming that there is no energy dissipation during fluid displacements, and all the pressure-volume work exerted by the pump to fill a pore is stored in the local fluid-fluid interfaces.

$$\cos\theta_t = \frac{2k\Delta V_w + \Delta A_{w,nw}}{\Delta A_{w,s}} \qquad \textit{Equation 3}$$

here, k is the curvature of the fluid/fluid interface immediately prior to displacement, ΔV_w is the change in volume of wetting fluid, $\Delta A_{w,nw}$ is the change in surface area of the fluid/fluid interface, $\Delta A_{w,s}$ is the change in the wetting fluid/solid surface area and θ_t is the thermodynamic contact angle

linked to the displacement. The surface areas were calculated by using the extracted triangulated surface described in Curvature measurements, where the methodology for determining k can also be found.

C. Pc determination

Image-based Pc values were determined from local menisci curvatures as the local Pc determines the curvature of the fluid meniscus according to the Young-Laplace equation. The invasion-Pc values predicted by the PNMs described above were validated against these local image-based Pc values.

i. Curvature-based Pc

Assuming the fluids are at quasi-equilibrium, the curvature of the fluid-fluid interface at the time of displacement (k_{thr}) can be used to calculate the capillary pressure over the interface using the Young Laplace equation (Equation 4) and the interfacial tension (Table 1). We use the local image-based Pc values determined by this method to validate the invasion-Pc values calculated from the PNMs.

$$Pc = 2\sigma k_{thr} \qquad \textit{Equation 4}$$

ii.Model implementation

Displacements were identified and categorised during the image analysis, after which the different PNMs were used to estimate at which invasion-Pc values those displacements occurred. Because we determined the local fluid arrangement before each fluid invasion from the µCT images, we did not need to perform an entire PNM simulation to predict the invasion-Pc values that each displacement would occur at. For piston-like displacements, we used the local geometric contact angles and source pore radius to estimate the invasion-Pc. For cooperative pore-fillings, we again used the local geometric contact angles and source pore radius, as well as the filling states of the neighbouring throats, their relative position and their radii. Finally, in order to predict the invasion-Pc of snap-offs, we used the local geometric contact angles during imbibition and drainage as well as the throat radius; angles of the corners of the throat; and the maximum curvature obtained during the preceding drainage.

IV.Results and Discussion

A. Contact angles

By detecting changes in pore and throat occupancy during the experiment, we identified 146 distinct imbibition displacements. These displacements were used to calculate local contact angles in three different ways (Figure 5). We also determined the geometric contact angles as these have been used in several wettability studies[49–51]. Of the four, the distribution of the local geometric contact angles was narrowest, as is evident in Figure 5 and the standard deviations in Table 2. This may suggest that the local geometric contact angles better account for the dynamics of the interface motion (such as hinging of pinned contact angles, hysteresis, interface relaxation, etc.) than the other types[18]. In this work, we investigate invasion-Pc linked to meniscus movements, hence it follows that the type of contact angle used must be equally local. For these reasons, the local geometric contact angles were selected for use as inputs in the PNMs in the following sections. To validate these measurements, manual geometric contact angles were determined in 6 randomly selected contact line points in the image[52]. Five were in good agreement with the results of the automated geometric contact angles in the same location, varying by 3˚ or less, with only one manual measurement differing from the automated value by 15˚.

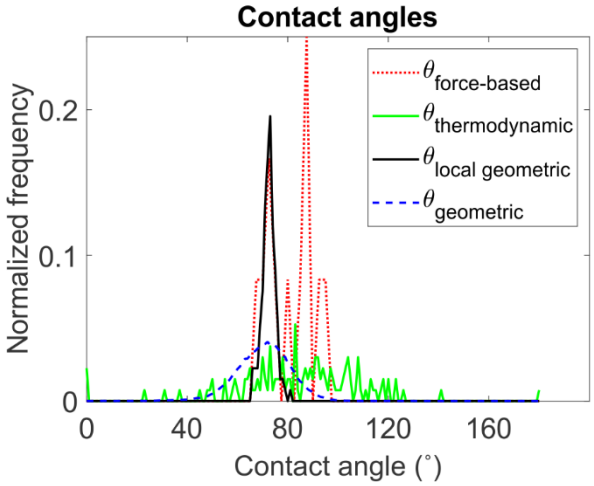

Figure 5: A frequency distribution plot of different types of contact angles. The force-based, thermodynamic and local geometric contact angles are measured locally in both space and time, while the geometric contact angles are measured on the final timestep of the experiment. The local geometric contact angles have the narrowest distribution, suggesting they are most suitable to use in the PNMs.

Table 2: Means and standard deviations of different types of contact angles.

Contact angle type	Mean (°)	Standard deviation (°)
Local geometric	72	2.6
Conventional geometric	70	10.9
Thermodynamic	85	23.8
Force-based	81	9.5

B. Validation of image-based curvatures

To assess the reliability of the meniscus curvatures from the µCT images, these values were compared to the average Pc measured with a pressure transducer[6] (referred to as Pressure transducer reading in Figure 6). The presence of pendular rings, as described in Armstrong et al.[6], may account for the mismatch between local image-based Pc and externally measured average Pc seen at higher saturations. Curvature measurements on pendular rings commonly lead to severe underestimation of the capillary pressure, as their small size makes them sensitive to segmentation errors which can cause the improper reversal of curvature values from positive to negative[6]. Some scatter of the local image-based Pc around the experimental measurements was expected due to local variations in the pressure difference, as the fluids were not in equilibrium during the imbibition process[37]. The finite image resolution and the image analysis further added to uncertainty. Akai et al.[53] postulated that the local image-based Pc could be estimated to within 11% if the average radius of curvature is at least 10 times the image resolution. This radius of curvature equated to a Pc of ~0.4 kPa in this study. Since pressure transducer readings were close to this value, the spatial resolution likely influenced the results, especially at lower wetting phase saturations, where the radii of curvatures were lower (due to the higher Pc values)[18]. The limited temporal resolution added to the uncertainty because the curvatures were determined tens of seconds before the fluid displacements occurred. The average rate of change of the pressure transducer readings was ~3Pa per timestep, which yields an uncertainty of ~4% on the average local image-based Pc solely due to temporal resolution. Furthermore, this limitation also caused motion artefacts in the images[27].

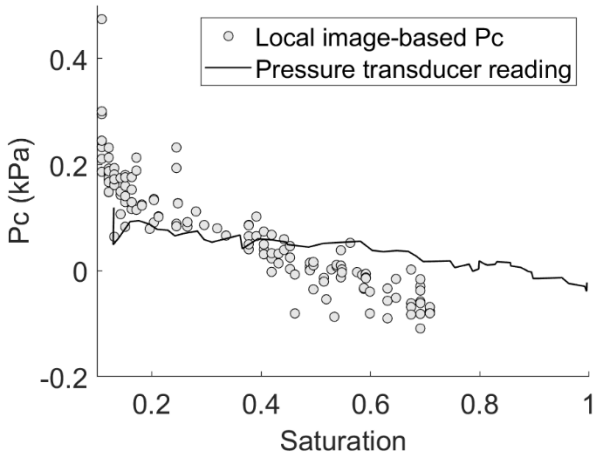

Figure 6: Local image-based Pc based on curvature measurements and pressure transducer readings plotted against wetting fluid saturation.

C. Fluid displacements

1. Piston-like fillings

Of the 146 distinct displacements detected, 12 were classified as piston-like. For these displacements, the predicted invasion-Pc values followed the same trend as the local image-based values and the pressure transducer readings (Figure 7): they decreased with increasing saturation, conforming to the conventional Pc imbibition curve[33]. However, the predicted invasion-Pc values were larger than the pressure transducer readings (Figure 8). This disparity was observed with both pore network extraction methods (Figure 7), suggesting a systematic error.

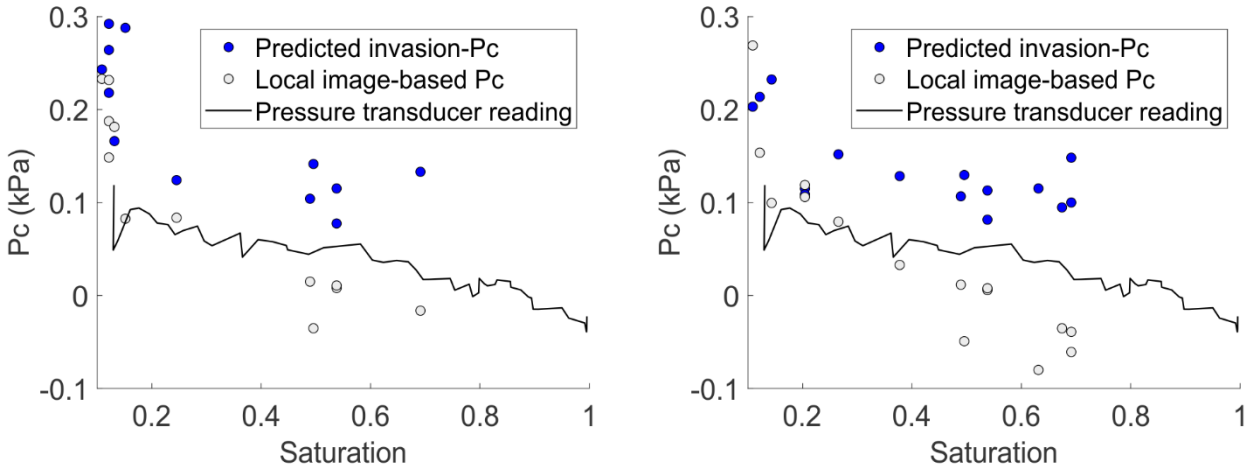

Figure 7: Predicted invasion-Pc based on the two different PNM structures for piston-like displacements plotted against saturation, compared with the local image-based Pc based on curvature measurements and the pressure transducer readings. The left was obtained using the maximum inscribed sphere pore network extraction method and the right using a watershed segmentation.

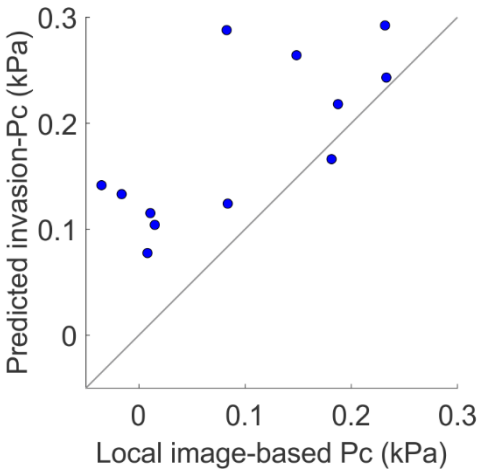

Figure 8: Predicted invasion-Pc plotted against local image-based Pc.

Visual inspection of these displacements revealed that six occurred at the edge of the field of view (e.g. Figure 9 A) and thus no conclusions could be drawn from them. It further revealed that one displacement was in reality a cooperative pore filling that spanned two pores (Figure 9 B). The maximum inscribed sphere of the throat between the two pores was brine filled, yet in the region of the throat not encompassed by the sphere, oil was present. This hints at the difficulties of the PNM structure to allow the model to capture the intricacies of displacements spanning multiple pores. In this case, the interface configuration in the throat is what we traditionally expect to see in a pore, hence the model cannot recognise it as a cooperative pore filling, due to the way the pore space is parameterized.

Visualizing the remaining five displacements revealed that the overestimation of the predicted invasion-Pc likely stemmed from difficulties the network structures have to accurately describe the pore space (Figure 9 C and D). Firstly, both network extractions overseparated the pore space: single pores were erroneously split into several pores (Figure 9 C). This yielded an underestimation of the radius used in the Young Laplace equation, resulting in higher than expected invasion-Pc values. At lower saturations, the invasion-Pc values were closer to the local image-based values and pressure transducer readings than at higher saturations. This was likely due to the fact that smaller pores were invaded first, and these pores were less likely to be over-separated than the larger pores filled later. Secondly, the radius used in the Young-Laplace equation was derived from the maximum inscribed sphere of the pore. This value was likely smaller than the maximum mean radius of curvature a meniscus could assume in irregularly shaped pores (Figure 9 D), again leading to higher than expected invasion-Pc values. These issues suggest that the network extraction methods struggled with describing the geometrical properties of the pore space of the sample in this case study.

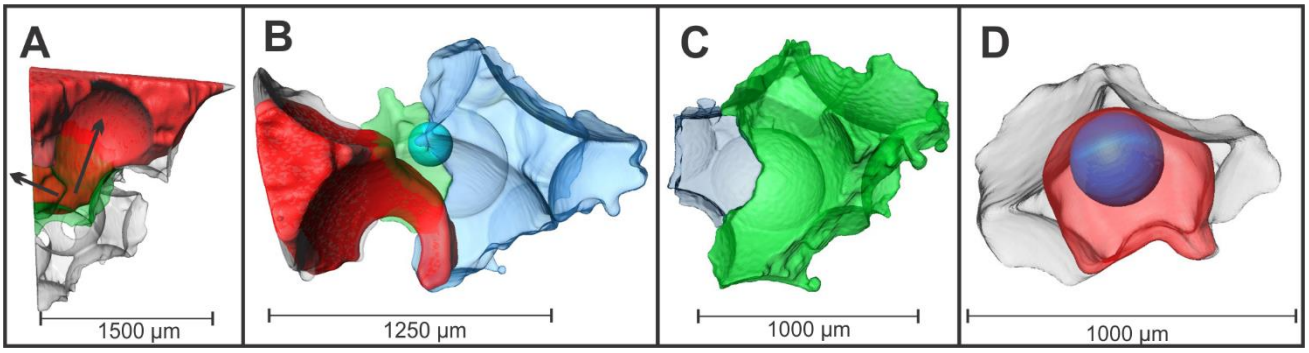

Figure 9: A) The oil in the green (middle) pore can escape in the direction of the left arrow or the right arrow. The right arrow's path is captured by the maximum inscribed sphere of the throat between the green pore and its neighbour, but there is no throat assigned at the location of the left arrow since it leads to outside the field of view. We can therefore make no conclusions from this displacement. B) The throat between the green pore (left) and the blue pore (right) is represented by the blue ball at their boundaries. The filling state of that ball determines whether the throat is classified as containing oil or brine. Since the ball is devoid of oil, this throat was classified as brine filled, whereas there is oil in the lower part of the throat. C) An over-separated pore. The pore network extraction results in what should be one pore being split into the green (right) and blue (left) pores. D) The radius of curvature of the inscribed sphere (blue) is smaller than the radius of curvature of the oil protrusion (transparent red) within the pore (grey).

Another possible source of mismatch is the quasi-static nature of the PNM, meaning it does not intrinsically account for dynamic effects which occur during imbibition. While the experiment was unsteady-state[18], the capillary number of the flow was 10^{-8}, ensuring the fluids remained near hydraulic equilibrium[27]. Despite the low capillary number, viscous dynamic effects could further explain the mismatch between the prediction and the measurement. Individual displacements during imbibition have been shown to occur at high velocities, resulting in large local viscous forces, even when the average flow velocity is low and the capillary number hence indicates a capillary dominated flow[21].

For some displacements, the predicted invasion-Pc is higher than the displacements near them in terms of saturation, while their local image-based Pc is lower than those near to them. Also, some displacements have invasion-Pc values higher than displacements which were identified at lower saturations. This means the PNM would have predicted a different filling sequence than the one identified by the image analysis and curvature measurements. This inconsistency will in turn affect the constitutive properties predicted by the PNM.

2. Cooperative pore-filling

Of the 121 cooperative pore-fillings identified, 68 were one pore in size and could therefore be compared to model predictions (the model is not valid for displacements where multiple neighbouring pores are filled at the same time). Using both PNM structures, the predicted invasion-Pc values for these events were all negative and fell below the local image-based Pc values (Figure 10). Capillary pressure curves in quasi-static PNM are calculated as the minimum capillary pressure needed to perform all the invasion up to a certain saturation, and the predictions are thus poor. Since invasion-percolation fills accessible network elements in the order of decreasing invasion Pc, this means that the model would not expect the experimentally observed displacements to take place. The mismatch between the model and the experiment could be explained, at least in part, by taking into account the limited time resolution of the experiment: the invasions that appeared to be cooperative pore fillings could actually have taken place as a rapid succession of several displacements. This would entail one or more snap-offs occurring in the throats neighbouring the pore in question, quickly followed by a lower order cooperative pore-filling or piston-like displacement made accessible by the snap-off's alteration of the local fluid distribution. In an invasion-percolation framework, this sequential event would be more likely than the initially identified cooperative pore filling if the invasion-Pc of one or more snap-offs in the surrounding throats were higher than that of the latter.

To test the impact of the possible occurrence of fast sequential events on the match between model and experiment, we calculated the invasion-Pc values of snap-offs surrounding the pores. Once the likelihoods of the snap-offs were confirmed, we recalculated the invasion-Pc values of the pores using the updated fluid configurations; e.g. if snap-off in a throat had a higher invasion Pc than the cooperative pore filling, then that throat was reclassified as brine-filled, and the cooperative pore filling pressure for the neighbouring pore was recalculated. We found that the predicted invasion-Pc values for the snap-offs typically had high values (Figure 10), suggesting that the model would predict them to occur. After simulating between one and seven snap-offs around each pore (Table 3), the predicted invasion-Pc values matched better to the local image-based Pc values and pressure

transducer readings (Figure 11). Nevertheless, there was still scatter, which would cause the predicted invasion sequence to be different than the experimentally measured one, which could have an impact on the resulting constitutive properties that the model would predict. The predicted invasion-Pc values were again greater than the local image-based Pc values (Figure 11). The reasons for mismatch between the model and the experiment are likely the same as for the mismatch in the piston-like displacements: the pore separation methods were unable to accurately describe the pore space and the quasi-static nature of the model failed to capture dynamic effects sufficiently.

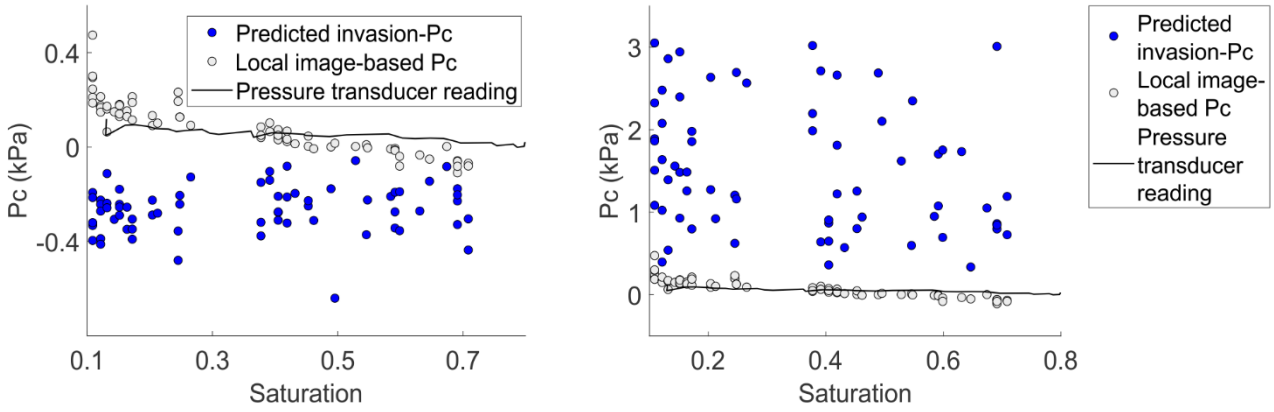

Figure 10: (Left) Predicted invasion-Pc for cooperative pore-fillings plotted against saturation, compared with the local image-based Pc and the pressure transducer readings. (Right) Predicted invasion-Pc of snap-offs simulated around pores assumed to be filled by cooperative pore-fillings. According to percolation invasion, since they are greater than the local image-based Pc and pressure transducer readings, they are predicted to be likely to occur.

Table 3: Number of snap-offs simulated and the corresponding number of pores where predicted invasion-Pc has just become greater than (or near to) local image-based Pc.

Number of snap-offs	Number of pores where predicted invasion-Pc has just become greater than local image-based Pc
1	27
2	20
3	13
4-7	8

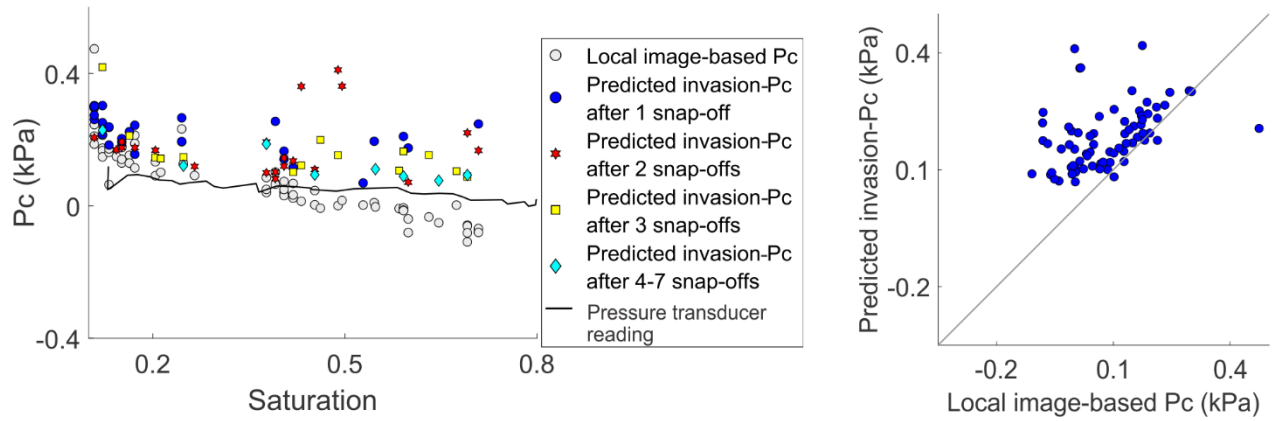

Figure 11: This graph shows the results after snap-offs were simulated. Predicted invasion-Pc for cooperative pore-fillings plotted against saturation, compared with the local image-based Pc and the pressure transducer readings.

If we assume the sequential filling approach outlined above to be realistic, we found that there were 147 snap-offs, 64 piston-like displacements and 4 cooperative pore-fillings (Figure 12). This dominance of piston-like displacements compared to cooperative pore fillings agrees partly with the findings of Singh et al.[54] who reported 68% piston-like displacements and only 22% I_2 cooperative pore-fillings when analysing capillary dominated imbibition in a Ketton limestone rock sample. Our findings showed a much higher proportion of piston-like displacements compared to cooperative pore-fillings than Singh et al.[54], however. Singh et al.[54] also found a lower percentage of snap-offs (~7% of displacements), despite the typically higher aspect ratios in Ketton limestone compared to a glass bead pack. This could be due to misidentification of fast sequential events in the former, as they suffered from similar time resolution constraints as the experimental data presented here.

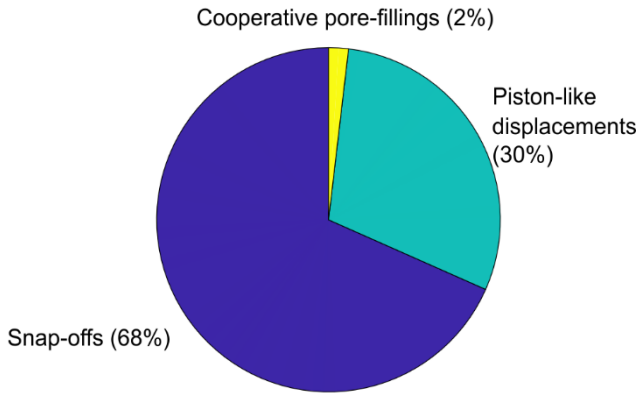

Figure 12: Proportions of the different types of displacements assuming the sequential filling approach is realistic. The original 68 single pore cooperative pore-fillings were thus found to be this combination of different displacement types.

3. Snap-off

Of the 13 snap-offs identified by the image analysis, one was eliminated as an outlier as it had a predicted invasion-Pc several orders of magnitude larger than that of the other snap-offs. The invasion-Pc values followed the expected trend of decreasing Pc with increasing saturation (Figure 13). However, this trend was not visible in the local image-based Pc values, likely due to scatter. The local image-based Pc values of snap-offs are most difficult to estimate as there are no terminal menisci on which to make curvature measurements before the displacement. Instead measurements were made in the timestep after the displacement, increasing the uncertainty of the measurement. The predicted invasion-Pc values were greater than the local image-based Pc values, suggesting that the PNM would predict that they would occur. However, the PNM would predict these snap-offs to occur earlier than the image analysis found (since according to invasion percolation, displacements which have a higher invasion-Pc occur earlier). The predicted invasion-Pc values were a poor match for local image-based values and pressure transducer readings. The low temporal resolution may contribute to the mismatch. The mismatch may also be due to the flow not being at capillary equilibrium. In order to study this, we investigated the temporal and spatial locations of the snap-offs.

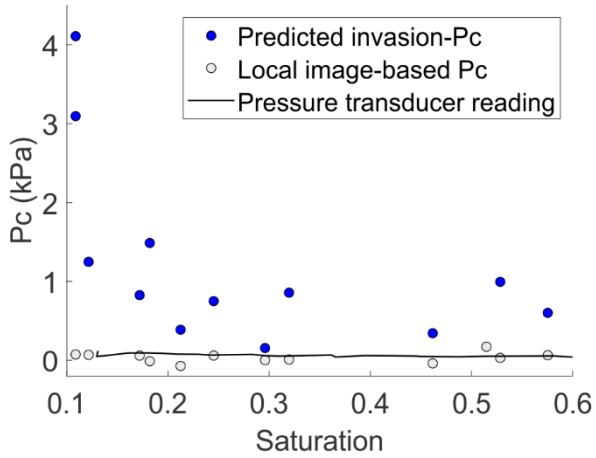

Figure 13: Predicted invasion-Pc for snap-offs plotted against saturation, compared with the local image-based Pc and the pressure transducer readings.

Snap-offs which occurred closer to the inlet happened earlier in the experiment and at lower saturations (Figure 14). However, there is no increasing trend in the predicted invasion-Pc with the length along the sample. These results make sense when considering that brine must flow through films from the inlet to the location of the snap-off. This means that snap-offs at locations further from the inlet would happen later, and thus at higher saturation and lower invasion-Pc. These trends thus reflect that the sample was not at capillary equilibrium, and can thus not be captured by quasi-static models[33,37].

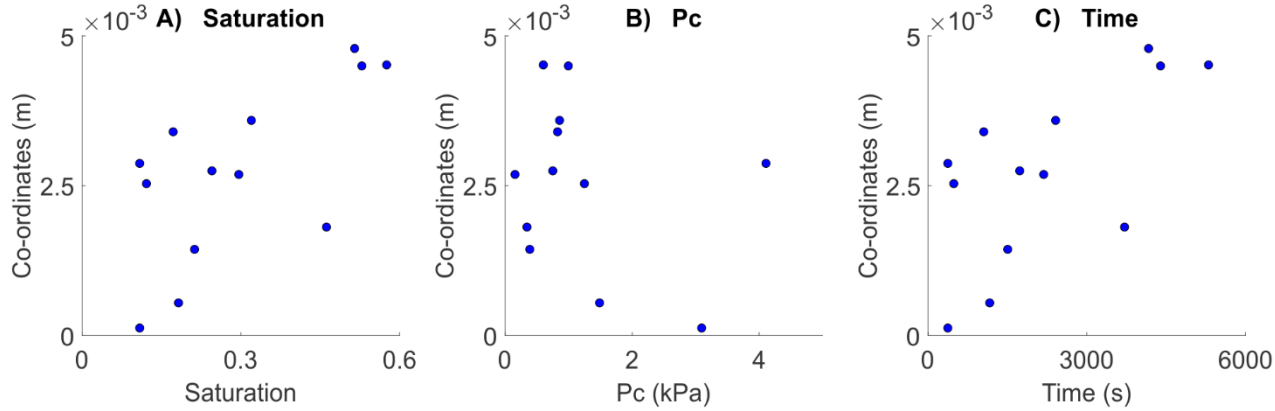

Figure 14: Saturation, predicted invasion-Pc and time plotted against distance from the inlet for each snap-off identified in the image analysis.

V.Conclusion

In this work, we developed a workflow to validate models of imbibition using invasion-Pc, which dictates the sequence in which the pore-filling process occurs. We did this by comparing invasion-Pc values predicted by PNMs of piston-like displacements, cooperative pore-fillings and snap-offs to local image-based Pc values calculated from meniscus curvatures extracted from µCT images. We considered two different PNM extraction methods from a dry µCT scan of the sample and several methods to calculate the local contact angles as input to the model. Using this workflow on a µCT dataset of imbibition in a glass bead pack allowed us to pin down several causes of error in these PNMs.

The invasion-Pc values predicted by the PNMs of piston-like displacements were all greater than the local image-based Pc values. Possible reasons for this include: uncertainties in the experimental

analysis of the data, difficulties of the used network extraction methods to accurately describe the pore space geometry and viscous/dynamic effects. Due to the relatively low temporal resolution, we worked under the assumption that sequential events were realistic and saw the same trends in the invasion-Pc values predicted for cooperative pore-fillings as in the piston-like displacements. However, the PNM predicted that piston-like displacements were more plentiful than I_2 cooperative pore-fillings, aligning with the findings of Singh et al.[54]. This shows that while the PNM is capable of capturing the general prevalence of the different types of displacements, it fails to match predicted invasion-Pc values to local image-based Pc values for specific displacements. The PNM is sensitive to errors in the geometrical description of the pore space and is hence limited by the difficulties of the used network extraction methods to accurately describe this, as with piston-like displacements. This might be more problematic in the current bead back dataset than in pore geometries with higher constriction ratios, where throat surfaces may be more easily identified and where cooperative pore filling might play a less important role[55]. Finally, as the PNM is quasi-static in nature, viscous/dynamic effects likely also play a role. The predicted invasion-Pc values for snap-offs were again all greater than the local image-based Pc values. This may be attributed to the relatively low temporal resolution of the dataset and dynamic effects.

In order to accurately predict relative permeabilities and other constitutive properties, PNMs rely on the predicted invasion-Pc values in individual pores and throats, leading to the correct sequence in which displacements occur. The mismatch we see in our results indicates that the sequence of displacements predicted by the PNMs would not match the sequence identified by the experimental image analysis and hence the constitutive properties which they predict would likely be inaccurate. The method presented here may be used to guide the development of improved pore network extraction methods that better capture the link between local pore geometry and fluid invasions.

Acknowledgements

Dr. Steffen Schlüter is thanked for making his data available. Sharon Ellman is a PhD Fellow with the Research Foundation – Flanders (FWO) and acknowledges its support under grant 1182822N. T. Bultreys holds a senior postdoctoral fellowship from the Research Foundation-Flanders (FWO) under Grant No. 12X0922N. This research also received funding from the Research Foundation–Flanders under grant G051418N. The data used in this work is freely available online.

VI. References

1. Fetter, C. *Contaminant Hydrogeology*. (Prentice Hall, 1999).
2. Kota, A. K., Kwon, G., Choi, W., Mabry, J. M. & Tuteja, A. Hygro-responsive membranes for effective oilg-water separation. *Nat. Commun.* **3**, (2012).
3. Ma, J., Li, Q., Kühn, M. & Nakaten, N. Power-to-gas based subsurface energy storage: A review. *Renew. Sustain. Energy Rev.* **97**, 478–496 (2018).
4. Lackner, K. S. A Guide to CO2 Sequestration. *Science (80-.).* **300**, 1677–1678 (2003).
5. Benson, S. M. & Cole, D. R. CO2 sequestration in deep sedimentary formations. *Elements* **4**, 325–331 (2008).
6. Armstrong, R. T., Porter, M. L. & Wildenschild, D. Linking pore-scale interfacial curvature to column-scale capillary pressure. *Adv. Water Resour.* **46**, 55–62 (2012).
7. Bultreys, T., Singh, K., Raeini, A. Q., Ruspini, L. C., Øren, P.-E. P. E., Berg, S., Rücker, M., Bijeljic, B. & Blunt, M. J. Verifying Pore Network Models of Imbibition in Rocks Using Time-Resolved

Synchrotron Imaging. *Water Resour. Res.* **56**, 1–23 (2020).

8. Singh, K., Jung, M., Brinkmann, M. & Seemann, R. Capillary-dominated fluid displacement in porous media. *Annu. Rev. Fluid Mech.* **51**, 429–449 (2019).

9. Zhao, B., MacMinn, C. W. & Juanes, R. Wettability control on multiphase flow in patterned microfluidics. *Proc. Natl. Acad. Sci.* **113**, 10251–10256 (2016).

10. Bultreys, T., De Boever, W. & Cnudde, V. Imaging and image-based fluid transport modeling at the pore scale in geological materials: A practical introduction to the current state-of-the-art. *Earth-Science Rev.* **155**, 93–128 (2016).

11. Berg, S. *et al.* Connected pathway relative permeability from pore-scale imaging of imbibition. *Adv. Water Resour.* **90**, 24–35 (2016).

12. Liu, H., Kang, Q., Leonardi, C. R., Schmieschek, S., Narváez, A., Jones, B. D., Williams, J. R., Valocchi, A. J. & Harting, J. Multiphase lattice Boltzmann simulations for porous media applications: A review. *Comput. Geosci.* **20**, 777–805 (2016).

13. Valvatne, P. H. & Blunt, M. J. Predictive pore-scale modeling of two-phase flow in mixed wet media. *Water Resour. Res.* **40**, 1–21 (2004).

14. Bondino, I., Hamon, G., Kallel, W. & Kac, D. Relative Permeabilities From Simulation in 3D Rock Models and Equivalent Pore Networks: Critical Review and Way Forward. *Petrophysics - SPWLA J. Form. Eval. Reserv. Descr.* **54**, 538–546 (2013).

15. Blunt, M. J., Bijeljic, B., Dong, H., Gharbi, O., Iglauer, S., Mostaghimi, P., Paluszny, A. & Pentland, C. Pore-scale imaging and modelling. *Adv. Water Resour.* **51**, 197–216 (2013).

16. Bultreys, T., Lin, Q., Gao, Y., Raeini, A. Q., Alratrout, A., Bijeljic, B. & Blunt, M. J. Validation of model predictions of pore-scale fluid distributions during two-phase flow. *Phys. Rev. E* **97**, (2018).

17. Øren, P. E., Bakke, S. & Arntzen, O. J. Extending Predictive Capabilities to Network Models. *SPE J.* **3**, 324–335 (1998).

18. Mascini, A., Cnudde, V. & Bultreys, T. Event-based contact angle measurements inside porous media using time-resolved micro-computed tomography. *J. Colloid Interface Sci.* **572**, 354–363 (2020).

19. Berg, S. *et al.* Real-time 3D imaging of Haines jumps in porous media flow. *Proc. Natl. Acad. Sci. U. S. A.* **110**, 3755–3759 (2013).

20. Armstrong, R., Ott, H., Georgiadis, A., Rucker, M., Schwing, A. & Berg2, S. Subsecond pore-scale displacement processes and relaxation dynamics in multiphase flow. *Water Resour. Res.* **50**, 9162–9176 (2014).

21. Rücker, M. *et al.* From connected pathway flow to ganglion dynamics. *Geophys. Res. Lett.* **42**, 3888–3894 (2015).

22. Youssef, S., Deschamps, H., Dautriat, J., Rosenberg, E., Oughanem, R., Maire, E. & Mokso, R. 4D Imaging of Fluid Flow Dynamics in Natural Porous Media With Ultra-Fast X-Ray Microtomography. *Int. Symp. Core Anal.* 1–12 (2013).

23. Andrew, M., Bijeljic, B. & Blunt, M. J. Pore-scale contact angle measurements at reservoir conditions using X-ray microtomography. *Adv. Water Resour.* **68**, 24–31 (2014).

24. AlRatrout, A., Raeini, A. Q., Bijeljic, B. & Blunt, M. J. Automatic measurement of contact angle in pore-space images. *Adv. Water Resour.* **109**, 158–169 (2017).

25. Akai, T., Lin, Q., Bijeljic, B. & Blunt, M. J. Using energy balance to determine pore-scale wettability. *J. Colloid Interface Sci.* **576**, 486–495 (2020).

26. Bakke, S. & Øren, P. E. 3-D pore-scale modelling of sandstones and flow simulations in the pore networks. *SPE J.* **2**, 136–149 (1997).

27. Schlüter, S., Berg, S., Rücker, M., Armstrong, R. T., Vogel, H.-J., Hilfer, R. & Wildenschild, D. Pore-scale displacement mechanisms as a source of hysteresis for two-phase flow in porous media. *Water Resour. Res.* **52**, 2194–2205 (2016).

28. Gharbi, O. & Blunt, M. J. The impact of wettability and connectivity on relative permeability in carbonates: A pore network modeling analysis. *Water Resour. Res.* **48**, 1–14 (2012).

29. Raeesi, B. & Piri, M. The effects of wettability and trapping on relationships between interfacial area, capillary pressure and saturation in porous media: A pore-scale network modeling approach. *J. Hydrol.* **376**, 337–352 (2009).

30. Høiland, L. K., Spildo, K. & Skauge, A. Fluid flow properties for different classes of intermediate wettability as studied by network modelling. *Transp. Porous Media* **70**, 127–146 (2007).

31. Klise, K. A., Moriarty, D., Yoon, H. & Karpyn, Z. Automated contact angle estimation for three-dimensional X-ray microtomography data. *Adv. Water Resour.* **95**, 152–160 (2016).

32. Scanziani, A., Singh, K., Blunt, M. J. & Guadagnini, A. Automatic method for estimation of in situ effective contact angle from X-ray micro tomography images of two-phase flow in porous media. *J. Colloid Interface Sci.* **496**, 51–59 (2017).

33. Blunt, M. J. *Multiphase Flow in Permeable Media: A Pore-Scale Perspective*. *Multiphase Flow in Permeable Media* (2017). doi:10.1017/9781316145098.

34. Lenormand, R., Zarcone, C. & Sarr, A. *Mechanisms of the displacement of one fluid by another in a network of capillary ducts*. *Transport in Porous Media* vol. 83 337 (1983).

35. Singh, K., Bultreys, T., Raeini, A., Shams, M. & Blunt, M. Imbibition in porous media: correlations of displacement events with pore-throat geometry and the identification of a new type of pore snap-off. 1–12 (2019) doi:10.31223/osf.io/62gfr.

36. Haines, W. B. The hysteresis effect in capillary properties and the mode of moisture distribution associated therewith. *J. Agric. Sci.* **20**, 7 (1929).

37. Singh, K., Menke, H., Andrew, M., Lin, Q., Rau, C., Blunt, M. J. & Bijeljic, B. Dynamics of snap-off and pore-filling events during two-phase fluid flow in permeable media. *Sci. Rep.* **7**, 1–13 (2017).

38. Wilkinson, D. & Willemsen, J. F. Invasion percolation: a new form of percolation theory. *J. Phys. A. Math. Gen.* **16**, 3365 (1983).

39. Ruspini, L. C., Farokhpoor, R. & Øren, P. E. Pore-scale modeling of capillary trapping in water-wet porous media: A new cooperative pore-body filling model. *Adv. Water Resour.* **108**, 1–14 (2017).

40. See Supplemental Material at [URL will be inserted by publisher] for equations used in underlying models.

41. Raeini, A. Q., Bijeljic, B. & Blunt, M. J. Generalized network modeling of capillary-dominated two-phase flow. *Phys. Rev. E* **97**, (2018).

42. Gostick, J., Khan, Z., Tranter, T., Kok, M., Agnaou, M., Sadeghi, M. & Jervis, R. PoreSpy: A Python Toolkit for Quantitative Analysis of Porous Media Images. *J. Open Source Softw.* **4**,

1296 (2019).

43. Lorensen, W. E. & Cline, H. E. Marching cubes: A high resolution 3D surface construction algorithm. *Proc. 14th Annu. Conf. Comput. Graph. Interact. Tech. SIGGRAPH 1987* **21**, 163–169 (1987).

44. Li, T., Schlüter, S., Dragila, M. I. & Wildenschild, D. An improved method for estimating capillary pressure from 3D microtomography images and its application to the study of disconnected nonwetting phase. *Adv. Water Resour.* **114**, 249–260 (2018).

45. Dijkstra, E. W. A note on two problems in connexion with graphs. *Numer. Math.* **1**, 269–271 (1959).

46. Quéré, D. Wetting and roughness. *Annu. Rev. Mater. Res.* **38**, 71–99 (2008).

47. Khanamiri, H., Slotte, P. A. & Berg, C. F. Contact Angles in Two - Phase Flow Images. *Transp. Porous Media* **135**, 535–553 (2020).

48. Blunt, M. J., Lin, Q., Akai, T. & Bijeljic, B. A thermodynamically consistent characterization of wettability in porous media using high-resolution imaging. *J. Colloid Interface Sci.* **552**, 59–65 (2019).

49. Alhammadi, A. M., Alratrout, A., Singh, K., Bijeljic, B. & Blunt, M. J. In situ characterization of mixed-wettability in a reservoir rock at subsurface conditions. *Sci. Rep.* **7**, 1–9 (2017).

50. AlRatrout, A., Blunt, M. J. & Bijeljic, B. Spatial Correlation of Contact Angle and Curvature in Pore-Space Images. *Water Resour. Res.* **54**, 6133–6152 (2018).

51. AlRatrout, A., Blunt, M. J. & Bijeljic, B. Wettability in complex porous materials, the mixed-wet state, and its relationship to surface roughness. *Proc. Natl. Acad. Sci. U. S. A.* **115**, 8901–8906 (2018).

52. See Supplemental Material at [URL will be inserted by publisher] for an example of a manually measured geometric contact angle.

53. Akai, T., Lin, Q., Alhosani, A., Bijeljic, B. & Blunt, M. Quantification of Uncertainty and Best Practice in Computing Interfacial Curvature from Complex Pore Space Images. *Materials (Basel).* **12**, 2138 (2019).

54. Singh, K., Bultreys, T., Raeini, A. Q., Shams, M. & Blunt, M. J. New type of pore-snap-off and displacement correlations in imbibition. *J. Colloid Interface Sci.* **609**, 384–392 (2022).

55. Blunt, M., King, M. J. & Scher, H. Simulation and theory of two-phase flow in porous media. *Phys. Rev. A* **46**, 7680–7699 (1992).